Mon. Not. R. Astron. Soc. **000**, 1–12 (2009) Printed 30 November 2009 (MN LATEX style file v2.2)

X-ray groups and clusters of galaxies in the Subaru-XMM Deep Field

A. Finoguenov[1,2], M.G. Watson[3], M. Tanaka[4], C. Simpson[5], M. Cirasuolo[6], J.S. Dunlop[6], J.A. Peacock[6], D. Farrah[7], M. Akiyama[8], Y. Ueda[9], V. Smolčić[15], G. Stewart[3], S. Rawlings[10], C. van Breukelen[10], O. Almaini[11], L. Clewley[10], D.G. Bonfield[12], M.J. Jarvis[12], J.M. Barr[10], S. Foucaud[11], R.J. McLure[6], K. Sekiguchi[13], E. Egami[14]

[1] *Max-Planck-Institut für extraterrestrische Physik, Giessenbachstraße, 85748 Garching, Germany*
[2] *University of Maryland, Baltimore County, 1000 Hilltop Circle, Baltimore, MD 21250, USA*
[3] *X-ray Astronomy Group, Department of Physics and Astronomy, University of Leicester, Leicester LE1 7RH*
[4] *European Southern Observatory, Karl-Schwarzschild-Str 2, 85748, Garching, Germany*
[5] *Astrophysics Research Institute, Liverpool John Moores University, Twelve Quays House, Egerton Wharf, Birkenhead CH41 1LD*
[6] *Scottish Universities Physics Alliance, Institute for Astronomy, University of Edinburgh, Royal Observatory, Edinburgh EH9 3HJ*
[7] *Dept of Physics & Astronomy, University of Sussex, Falmer, Brighton, UK*
[8] *Astronomical Institute, Tohoku University, Sendai 980-8578, Japan*
[9] *Department of Astronomy, Kyoto University, Kyoto 606-8502, Japan*
[10] *Astrophysics, Department of Physics, Keble Road, Oxford OX1 3RH*
[11] *School of Physics and Astronomy, University of Nottingham, University Park, Nottingham NG7 2RD*
[12] *Centre for Astrophysics Research, Science & Technology Research Institute, University of Hertfordshire, Hatfield, AL10 9AB, UK*
[13] *Subaru Telescope, National Astronomical Observatory of Japan, 650 N. A'ohoku Place, Hilo, Hawaii 96720, USA*
[14] *Steward Observatory, University of Arizona, 933 N. Cherry Ave., Tucson, AZ 85721*
[15] *California Institute of Technology, MC 105-24, 1200 East California Boulevard, Pasadena, CA 91125*

subm. to MNRAS, Sep. 24 2009

ABSTRACT

We present the results of a search for galaxy clusters in Subaru-XMM Deep Field. We reach a depth for a total cluster flux in the 0.5–2 keV band of 2×10^{-15} ergs cm^{-2} s^{-1} over one of the widest XMM-Newton contiguous raster surveys, covering an area of 1.3 square degrees. Cluster candidates are identified through a wavelet detection of extended X-ray emission. The red sequence technique allows us to identify 57 cluster candidates. We report on the progress with the cluster spectroscopic follow-up and derive their properties based on the X-ray luminosity and cluster scaling relations. In addition, 3 sources are identified as X-ray counterparts of radio lobes, and in 3 further sources, X-ray counterpart of radio lobes provides a significant fraction of the total flux of the source. In the area covered by NIR data, our identification success rate achieves 86%. We detect a number of radio galaxies within our groups and for a luminosity-limited sample of radio galaxies we compute halo occupation statistics using a marked cluster mass function. We compare the cluster detection statistics in the SXDF with the predictions of concordance cosmology and current knowledge of the X-ray cluster properties, concluding that a reduction of concordance σ_8 value by 5% is required in order to match the prediction of the model and the data. This conclusion still needs verification through the completion of cluster follow-up.

Key words: cosmology: observations — cosmology: large scale structure of universe — cosmology: dark matter — surveys

1 INTRODUCTION

Extended X-ray emission from groups and clusters of galaxies is an unambiguous signal of high density, high mass environments (e.g. Borgani & Guzzo 2001, Rosati et al. 2002). The low scatter of X-ray emission around the mean with respect to the underlying mass of the object and advances in X-ray surveys, have established X-rays as one of the most reliable tools in the search for massive halos (e.g. Böhringer et al 2002). Deep XMM and Chandra surveys such as CDFS (Giacconi et al. 2002), CDFN (Bauer et al. 2002), Lockman Hole (Finoguenov et al. 2005), COSMOS (Finoguenov et al. 2007), XMM-LSS (Pacaud et al. 2007), CNOC2 (Finoguenov et al. 2009) show the potential of efficient group/cluster detection and

illustrate their competitiveness with spectroscopic group surveys. Such data have contributed directly to studies of galaxy formation (e.g. Tanaka et al. 2008; Giodini et al. 2009), Large Scale Structure (LSS) and its relation to AGN activity (Silverman et al. 2009), and have also shown the power of X-ray surveys to find and study sky densities in excess of 100 groups per square degree (Bauer et al. 2002).

At high redshifts, deep X-ray surveys offer both the highest sensitivity towards the cluster mass and are competitive to the best optical surveys for finding groups. Clusters at different redshifts provide homogeneous samples of galaxies in a high-density environment, enabling studies of the evolution of stellar populations (e.g. Blakeslee et al. 2003, Lidman et al. 2004, Mei et al. 2006, Strazzullo et al. 2006). Current results from the deep NIR fields indicate a strong evolution in galaxy color segregation near redshift 1.7 (Cirasuolo et al. 2007). Deep X-ray surveys of the same fields are therefore of further importance to provide the direct evidence of the role of groups and clusters of galaxies in cosmic galaxy build up.

This paper concentrates on cataloging and analysis of the statistical properties of the X-ray clusters primarily detected in XMM observations of the Subaru XMM Deep Field. The basic X-ray data reduction and a construction of the catalog of extended sources is discussed in §2. In §3 we describe the cluster identification using a refined red sequence method by including a galaxy preselection using multi-band photometric redshift catalog. The stand of the spectroscopic follow-up is presented in §4. In §5 we provide a final catalog of identified clusters, including the results of the spectroscopic follow-up. This is the first X-ray survey where special care is paid to select out the systems where extended X-ray emission is caused by radio lobes. The details and the results of this procedure are outlined in §5.1. Statistical properties of the clean X-ray cluster sample are discussed at the end of §5. §6 concludes the paper.

All through this paper, we adopt a "concordance" cosmological model, with $H_o = 72\,\mathrm{km\,s^{-1}\,Mpc^{-1}}$, $\Omega_M = 0.25$, $\Omega_\Lambda = 0.75$ (Komatsu et al. 2009), and — unless specified — quote all X-ray fluxes in the [0.5–2] keV band and rest-frame luminosities in the [0.1–2.4] keV band and provide confidence intervals at the 68% level.

2 XMM DATA REDUCTION

The SXDF incorporates a deep, large-area X-ray mosaic with XMM-Newton, consisting of seven overlapping pointings covering 1.3 $\square^\circ$ region of the high Galactic latitude sky with an exposure time of 100 ks in the central field (in separate exposures) and 50 ks in the flanking fields (for details see Geach et al. 2007). Four of the pointings were carried out in 2000 August, and the remaining three were made in August 2002 and January 2003.

For cluster detection, we used the XMM-Newton mosaic image in the 0.5–2 keV band, consisting of 7 pointings, 400 ksec in total. A description of the XMM-Newton observatory is given by Jansen et al. (2001). In this paper we use the data collected by the European Photon Imaging Cameras (EPIC): the *pn*-CCD camera (Strüder et al. 2001) and the MOS-CCD cameras (Turner et al. 2001). All Epic-*pn* observations have been performed using the Thin filter, while both Epic-MOS cameras used the Medium filter.

In addition to the standard data processing of the EPIC data, which was done using XMMSAS version 6.5 (Watson et al. 2001; Kirsch et al. 2004; Saxton et al. 2005), we perform a more conservative removal of time intervals affected by solar flares, following the procedure described in Zhang et al. (2004). In order to increase our capability of detecting extended, low surface brightness features, we have applied the 'quadruple background subtraction' (Finoguenov et al. 2007) and also check for high background that can be present in a few MOS chips (Snowden et al. 2008), identifying none. The resulting countrate-to-flux conversion in the 0.5–2 keV band excluding the lines is 1.59×10^{-12} for *pn* and 5.41×10^{-12} for each MOS detector, calculated for the source spectrum, corresponding to the APEC (Smith et al. 2001) model for a collisional plasma of 2 keV temperature, 1/3 solar abundance and a redshift of 0.2. We note that in reconstructing the properties of the identified groups and clusters of galaxies, we implement the exact corrections, based on the source spectral shape (as defined by the expected temperature of the emission) and the measured redshift of the system.

After the background has been estimated for each observation and each instrument separately, we produce the final mosaic of cleaned images and correct it for the mosaic of the exposure maps in which we account for differences in sensitivity between pn & MOS detectors.

We use the prescription of Finoguenov et al. (2009) for extended source detection, which consists in removal the PSF model for each detected point source from the data before applying the extended source search algorithm. The signal-to-noise ratio image of the point-source cleaned image is shown in Fig. 1. As can be seen from the figure, the image exhibits a fairly uniform signal-to-noise ratio. Without the refined background subtraction, the signal-to-noise image exhibited large-scale variations, which could mimic an extended source. On the image, the ellipses show the position and the angular extent of detected sources. The total number of extended sources detected is 84. Identification of sources required to split several sources, increasing the total to 92. The threshold for the wavelet source detection has been set to 4 standard deviations. The calibrated map of the wavelet noise (Vikhlinin et al. 1998) has been produced and used for modelling of the survey sensitivity. The extent of the source, which we used for identification and flux estimates, has been followed down to 1.6 times the local wavelet noise value. The significance of the flux estimate can be lower than 4 sigma. This is due to both a change in the significance of the source between the peak of its significance and its extent as well as a difference in the error field for detection and flux extraction. The later difference is driven by difference in the fluctuation level between the wavelet noise (important for detection) and unsmoothed source+noise (important for the flux estimate). These differences decrease with the increasing exposure of the survey (and e.g., are gone in our analysis of CDFS (Finoguenov et al. in prep.). Apart from the allowance for systematical errors associated with AGN removal lately, the procedures of calculating the sensitivity maps are the same as in Finoguenov et al. (2007). Prior removal of point sources simplifies the extended flux estimate and also allows us to use the X-ray center of extended emission as a prior for identification, as detailed below. A small fraction of sources ($\sim 15\%$) remains unidentified even in the area with best follow-up data. Only 6% can be accounted for by remaining deficiencies with the source identification (see below). We believe this can be an effect associated with joined detection of a number of sub-threshold point sources (e.g. Burenin et al. 2007). A study of the origin of this source population is on-going using CDFS and CDFN data, where one can profit from Chandra resolution (Finoguenov et al. in prep.).

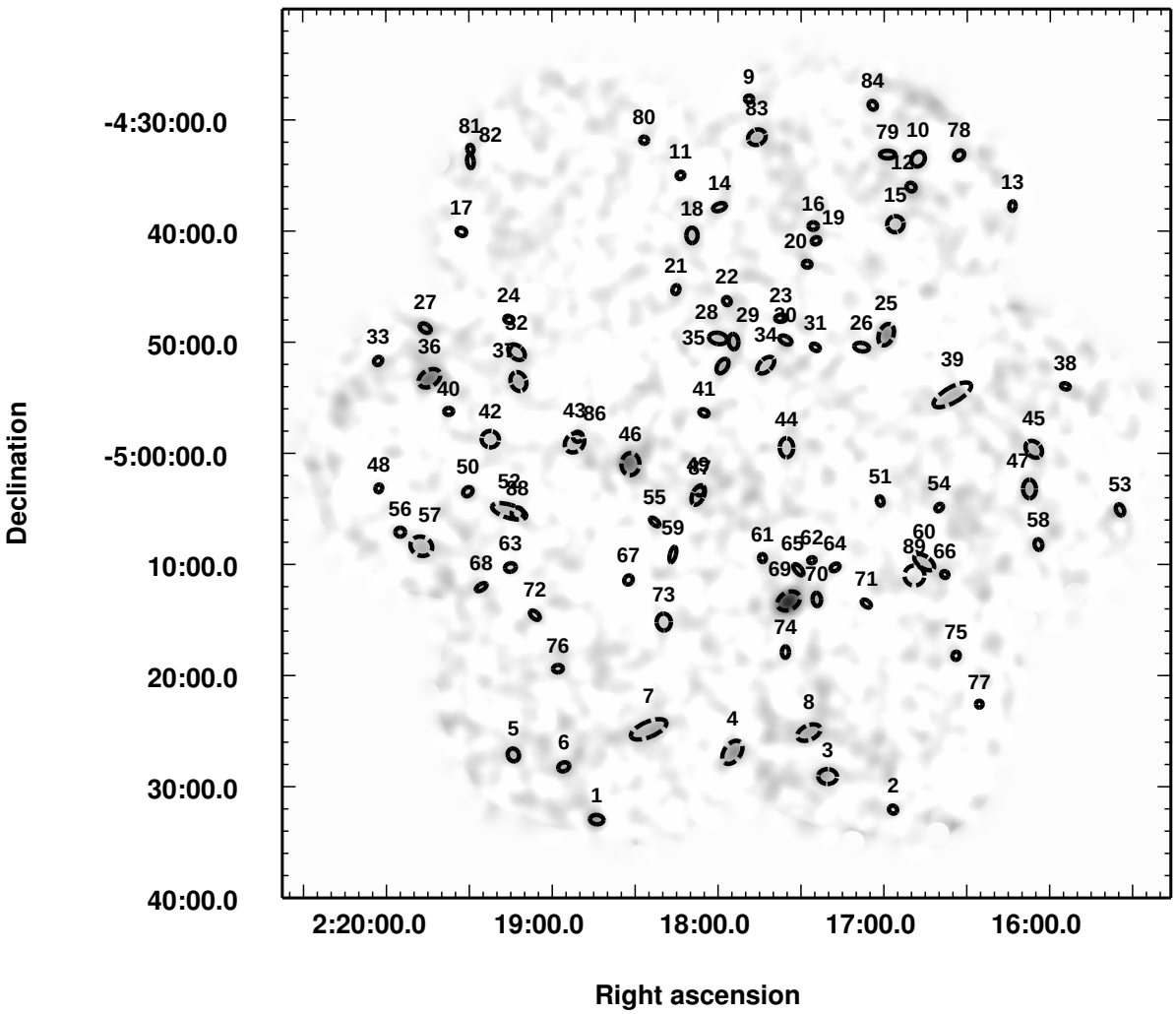

Figure 1. An image of the signal-to-noise ratio in the 0.5–2 keV band after background subtraction and point source removal. The image has been smoothed with a Gaussian of $32''$ width. White color corresponds to the values smaller than 0, grey color starts at 1 sigma and black color corresponds to detection significance of 6 sigma per 200 square arcsecond element. Ellipses indicate the wavelet sources, labeled according to the catalog. The coordinate grid is for the Equinox 2000.

3 REFINED RED SEQUENCE TECHNIQUE FOR CLUSTER IDENTIFICATION

As a primary method for cluster identification we used the refined red sequence technique, described in this section. This is a further refinement of the photo-z concentration technique, used in Finoguenov et al. (2007). Uncertainty, related to identification of clusters based on the photo-z data alone has been addressed in van Breukelen et al. (2007). We deem our technique as the most robust cluster identification when only broad band photometric data are available. With the refinements, described here, this technique is also sensitive to identification of galaxy groups. However, strongly star-forming galaxy groups can not be detected through such techniques. This point is thoroughly checked using zCOSMOS survey, yielding only 1% of such systems (Finoguenov et al. in prep.), which are located at $z < 0.3$. As we discuss below, our identification at $z < 0.3$ is anyway not complete, due to lack of U-band photometry.

First we consider the calibration of the model red sequence, then we detail the application procedure and describe selection criteria. To model the evolution of the red sequence, we adopt the passive evolution model of a single stellar population (SSP), assuming no dust extinction, using the Bruzual & Charlot (2003) population synthesis code. In order to reproduce the slope of the red sequence, the red sequence in the Coma cluster (Bower, Lucey & Ellis 1992) has been fitted by the SSP models formed at $z_f = 5$ with various metallicities. Model galaxies are 'calibrated' in this way (Lidman et al. 2008). The model red sequence can then be evolved back in time to arbitrary redshifts. Note that this modeling is based on the assumption that the slope of the red sequence is entirely due to the mass-metalicity relation, as suggested both by observations and in theoretical work (e.g., Kodama & Arimoto 1997, Stanford et al. 1998).

The fitting procedure is three-fold. First, we extract galaxies in the area centered on the extended X-ray emission. We then estimate significance of an overdensity of red galaxies around the model red sequence at a given redshift. This procedure is performed at $0 < z < 2.5$. All significant (with details given in the following subsections) detections are stored for further consideration. As next we go through the step of approving the identifications. The results

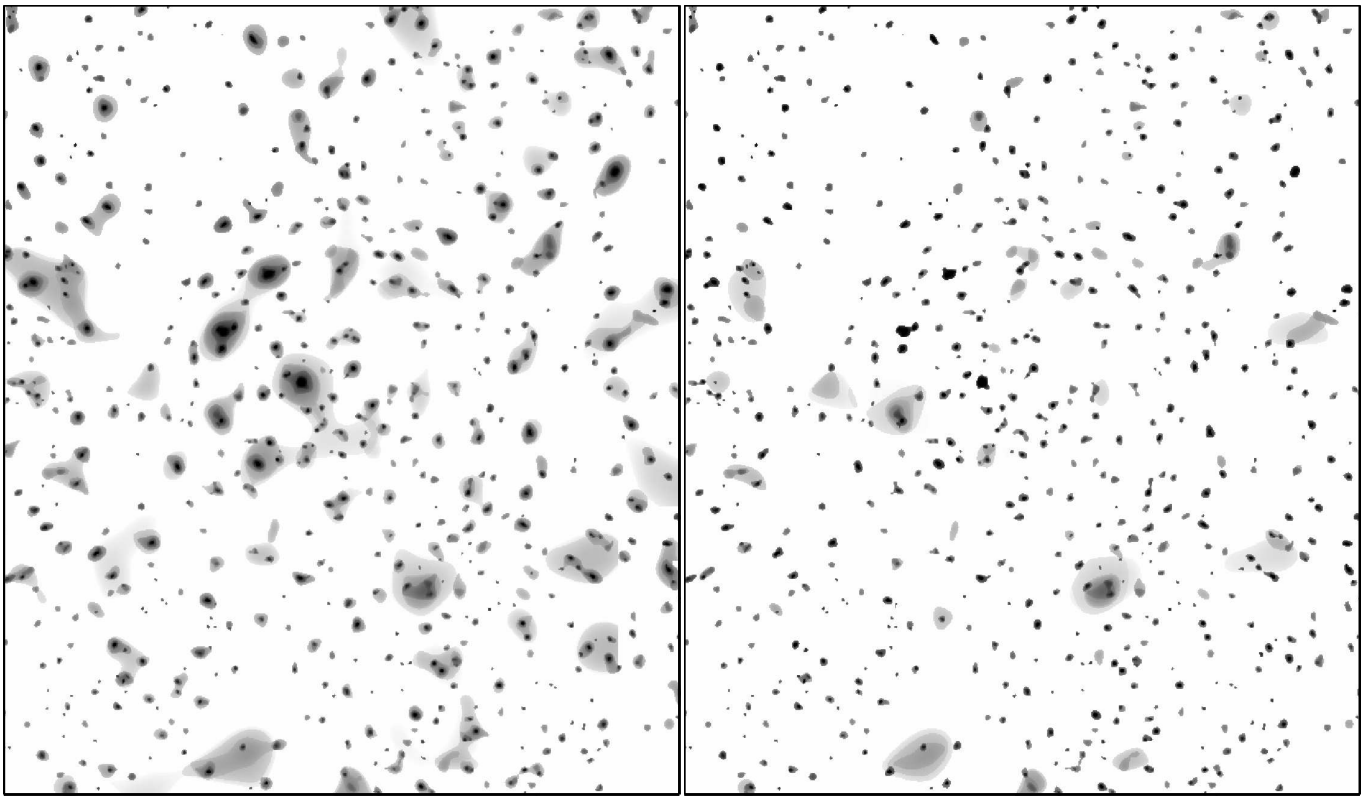

Figure 2. Comparison of two wavelet reconstructions of the SXDF field. *Left panel* displays a standard scale-wise decomposition, *right panel* includes a three-level subtraction of the PSF wings associated with the point-like sources, as described in the text. The scale limits for both images are the same. Clearly the left panel is much less diffuse. Both images are $45' \times 55'$. The pixel size is $4''$ on a side.

of spectroscopic follow-up of similar sources in CNOC2 field, discussed in Finoguenov et al. (2009), showed that the most reliable identification has more than 3 galaxies inside the X-ray shape of the source. In using the red sequence, to avoid chance projection a small dispersion of galaxies with respect to the model red sequence shall also be preferred. We therefore favor these identifications, even if they are not the most significant ones. When two or more identifications fit, we consider splitting the X-ray source according to the galaxy counterpart and check significance of these new sources, retaining only the significant ones and assigning a lower flag (=2), if such a procedure is impossible, the X-ray source is identified as confused (flag=4). Robust identifications have a clear concentration of red galaxies inside the detected X-ray emission. Some identifications are less obvious and require more follow-up work. These are marked correspondingly (flag=3). A comprehensive list of source flags is discussed in §5. Now we present the details of the method.

3.1 Construction of the photometric catalog

We use the Subaru $BVRiz$ photometric catalog from DR1 (Foucaud et al. 2007; Furusawa et al. 2008). The z-band selected catalog is used for this work. We also use JHK photometry from UKIDSS (UKIRT Infrared Deep Sky Survey) Ultra Deep Survey (UDS) Third Data Release (Warren et al. 2009). Objects from UDS are cross-correlated with the Subaru catalog. The catalog is further supplemented by Spitzer IRAC photometry from deep SpUDS program (PI James Dunlop) and Spitzer Wide-area InfraRed Extragalactic survey (SWIRE, Lonsdale et al. 2003). We use SExtractor to detect objects on the IRAC images and cross-correlate the IRAC objects with Subaru objects. We use $2''$ aperture for photometry and apply aperture correction. Since data from different telescopes have different PSF sizes, we use total magnitudes to derive colors. Stars are removed on the basis of their colors and compactness.

We then feed the catalog to our photometric redshift code. A detailed description of the code is given in Tanaka et al. (2008), but a brief outline is given here. The code uses a library of templates based on Bruzual & Charlot (2003) models. We assume the τ model to describe the star formation histories of galaxies and allow τ, dust extinction and intergalactic extinction to vary. Each observed object is fitted with all the templates and the best-fitting model is determined using the χ^2 statistics. The quality of the photometric redshift estimate has been compared to the spectroscopic redshifts, yielding 10% outliers ($|z_{phot} - z_{spec}| > 0.2$) and $0.03(1+z)$ uncertainty on redshift estimate below $z_{spec} = 4$. Dominant fraction of outliers is at $z < 0.3$ and is due to lack of U-band data.

3.2 Selection of Galaxies for cluster identification

As mentioned above, we go over the redshift (z) at which we apply the cluster red sequence method. We select galaxies at $|z - z_{phot}| < 0.2$, where z_{phot} is a photometric redshift. As next, we only consider the galaxies located within 0.5 Mpc (physical) from the center of X-ray emission at a given redshift (see description of Eq.1 below for more details of the weighting scheme). The aperture size is fixed on a physical scale and thus its apparent size on the sky varies with redshifts, at which we look for an over-density of red galaxies. This radius is wide enough to include most of the galaxies in

a candidate cluster, while it is small enough to detect weak signals from high redshift clusters.

Using a fixed aperture to select galaxies for the red sequence test is sufficient for our purposes as the probed mass range of systems in the survey is narrow and 0.5 Mpc typically encompasses r_{500} of the system. Alternative choice of galaxy selection can be either X-ray extent or an estimate of r_{500} based on the redshift guess and X-ray properties of the system. The X-ray extent is determined by statistical significance of the detection and would introduce uneven demand on matching between galaxies and the X-ray source. Furthermore, for nearby objects the extent of the emission is predicted to go into the scales where confusion becomes important ($2'$ for the depth of our survey), so the observed extent will be truncated. Using the fixed aperture, we can make a fair comparison of significance level of detection of overdensities at various redshifts.

3.3 Application of the red sequence method

To probe if there is any overdensity of red galaxies at a given redshift z, we count galaxies around the model red sequence. We use a Gaussian weight when counting galaxies in a form of

$$\sum_i \exp\left[-\left(\frac{color_{i,obs}-color_{model}(z)}{\sigma_{i,obs}}\right)^2\right] \times \exp\left[-\left(\frac{mag_{i,obs}-mag^*_{model}(z)}{\sigma_{mag}}\right)^2\right] \times \exp\left(-(\frac{r_i}{\sigma_r})^2\right), \quad (1)$$

where $color_{i,obs}$ and $mag_{i,obs}$ are the color and the magnitude of i-th observed galaxy, $\sigma_{i,obs}$ is the observed color error in $color_{i,obs}$, $color_{model}(z)$ is the model red sequence color at the magnitude of the observed galaxy, $mag^*_{model}(z)$ is the characteristic magnitude based on the model, which is tuned to roughly reproduce the observed characteristic magnitudes, σ_{mag} is the smoothing parameter detailed below, r_i is the distance from the X-ray center and σ_r is also a smoothing parameter as shown below. To account for systematic zero point errors in observations and for systematic magnitude/color errors in models, we take a minimum error in $\sigma_{i,obs}$ of 0.1 mag. For example, if an object has $\sigma_{i,obs} < 0.1$, we take $\sigma_{i,obs} = 0.1$ for this object.

Since different colors are sensitive to red galaxies at different redshifts, we adopt the following combination of colors and magnitudes.
$0.0 < z < 0.5 : B - i$ color and i magnitude
$0.5 < z < 1.0 : R - z$ color and z magnitude
$1.0 < z < 1.5 : i - K$ color and K magnitude
$1.5 < z < 2.5 : z - 3.6\mu m$ color and $3.6\mu m$ magnitude

In the Subaru/XMM Deep field, we have no U-band photometry, which is crucial for low-z red galaxies. Thus, our method is not very sensitive to clusters at $z < 0.3$ with estimated incompleteness in the cluster catalog of $\sim 6\%$.

The luminosity function of red galaxies varies with both richness of a cluster and redshift (Tanaka et al. 2005, 2007). To minimize the richness and redshift dependency of the red sequence technique, we weight galaxies according to their luminosity. This is implemented in the second term of Eq. 1, by adding high weight to the detection of bright red galaxies, adjusted according to passive evolution model, and the smoothing parameter σ_{mag}, which we set to a value of 2.

The third term in Eq. 1 takes into account the concentrations of galaxies. A galaxy at the center of the cluster has heavier weight than that in the outskirts. The relative weight as a function of distance from the center is controlled by the smoothing parameter σ_r. We take $\sigma_r = 1.0$ Mpc. This means that a galaxy at 0.5 Mpc from the center (i.e., galaxy at the edge of the extraction aperture) has a $e^{-0.25} = 0.78$ weight relative to a galaxy at the center. Altogether, we take into account the color evolution and the magnitude evolution of the red sequence (1st and 2nd term, respectively), the concentration of galaxies (3rd term) and a density of red galaxies around the red sequence at any given redshift.

To quantify the significance of the overdensity of red galaxies at the position of a cluster candidate, we put an aperture of the same size at a random position in the Subaru-XMM Deep Field and perform the same procedure 500,000 times. This gives an average number of red galaxies and its dispersion in the field at a given redshift. Then, the significance is evaluated as a relative overdensity of the cluster candidate to that of the field. A formal error of the red sequence redshift is not straight forward to estimate since we use many parameters to derive the significance and the absolute significance changes with these parameters. To remedy this complexity, we simply take the full-width at half maximum of the significance peak as the error. In Tab.1 we list the significance of the red sequence and the uncertainty of the redshift of the cluster.

4 SPECTROSCOPIC FOLLOW-UP

Since 2004 the $z < 1.3$ galaxy cluster candidates have been intensively followed up as part of a SXDF VLA program on VLT and targeted Gemini proposals (Simpson et al. 2006 and in prep.). Geach et al. (2007) reported multi-object spectroscopy on four candidate X-ray galaxy groups around moderate-luminosity radio sources. van Breukelen et al. (2007; 2009) report some of the results of Gemini program. Other spectroscopic observations of the field are reported in Yamada et al. (2005), Smail et al. (2008) and Akiyama et al. (2dF/AAOmega, in prep.). A total of 4k spectra have been obtained thus far.

Using the identification of the cluster with a red sequence method, we looked for spectroscopic redshifts of any of the red sequence galaxies. Where there has been a consistent spectroscopic redshift found, we considered it as a refinement. Next, we searched for more spectroscopic redshifts in all galaxies matching the selected redshift to $0.005 \times (1+z)$, which is twice a typical velocity dispersion. In addition we have also looked for galaxy clustering at different redshifts, when data allowed, but found no outliers. In the cluster catalog we report both the spectroscopic redshift when available and a number of galaxies used to derive it, which can be used to assess the quality of the spectroscopic follow-up.

In Tab.2 we list the coordinates and redshifts of the 144 galaxies assigned to the X-ray clusters. In case the cluster has less than 3 spectroscopic members, this assignment is tentative.

5 A CATALOG OF IDENTIFIED X-RAY CLUSTERS

In this section we describe our catalog of 57 X-ray galaxy clusters detected in the SXDF/UDS field. In the catalog (Tab.1) we provide the cluster identification number (column 1), R.A. and Decl.

of the peak of the galaxy concentration identified with the extended X-ray source in Equinox J2000.0 (2–3), photometric redshift (4). In case there are spectroscopic redshift determination for the cluster member galaxies, the median spectroscopic redshift is listed instead. The cluster flux in the 0.5–2 keV band is listed in column 5 with the corresponding 1 sigma errors. The flux has units of 10^{-14} ergs cm^{-2} s^{-1}. The rest-frame luminosity in the 0.1–2.4 keV band in units of 10^{42} ergs s^{-1} is given in (8). Column 9 lists the estimated total mass, M_{200}, computed following Rykoff et al. (2008) and assuming a standard evolution of scaling relations: $M_{200}E_z = f(L_X E_z^{-1})$. The corresponding R_{200} in arcminutes is given in column 10. Column 11 lists X-ray flag and the number of member galaxies inside R_{200}, $N(z)$ is given in column 12. The errors provided on the derived properties are only statistical and do not include the intrinsic scatter in the $L_X - M$ relation, which makes individual mass estimates uncertain by 0.2dex (Vikhlinin et al. 2009). To provide the insights on the reliability of both the source detection and the identification, in col (13) we provide the significance of the X-ray flux estimate and in col (14) the significance of the red sequence. Col. (15) shows the red sequence redshift and its uncertainty. Col. (16) provides the median photometric redshift of galaxies on red sequence. Finally, col. (17) provides a reference to the extended source catalog in Ueda et al. (2008).

Both flux estimates and the calculation of the properties of clusters are similar to the procedure outlined in Finoguenov et al. (2007). An X-ray quality flag (XFLAG) have been derived for the entire catalog based on visual inspection. XFLAG=1 is assigned to objects with high (in general > 6) significance of the X-ray flux estimate, and having a single optical counterpart. The next category of clusters (XFLAG=2), are low significance detections, for which X-ray centering has a large uncertainty (up to $30''$), hence a larger weight is given to the location of the optical counterpart. In addition, in cases when a single X-ray source has been split into several sources, matching the optical counterpart, the assigned flag is set equal 2 or larger. The clusters for which the photometric redshift of the optical or NIR counterpart is uncertain are flagged as XFLAG=3, which is mostly a concern at $z > 1.2$. XFLAG=4 indicates a presence of multiple optical counterparts, whose contribution to the observed X-ray emission is not possible to separate or rule out. Finally, the systems with potentially wrong assignment of an optical counterpart are marked as XFLAG=5.

In Ueda et al. (2008), the results of the analysis of the same XMM data has been presented, identifying a total of 32 extended sources. The extended sources were identified by examining source extent over the point spread function assuming a Gaussian as the intrinsic image profile. For extended sources considered in this paper, we search for sources from Ueda et al. (2008) catalog around the cluster central position within a radius of 32 arcsec, a typical size of significant extended emission. The positional errors (1σ) of the Ueda et al. (2008) sources are also taken into account in the matching. We recover 20 out of the 32 extended sources in Ueda et al. (2008) and identify 15 of them as clusters. In Tab.1 we provide a match between our cluster catalog and the extended sources in Ueda et al. (2008). The remaining differences can be understood as different sensitivities of the algorithm to extent of X-ray emission, which in our case is taken into account in the modelling of the survey.

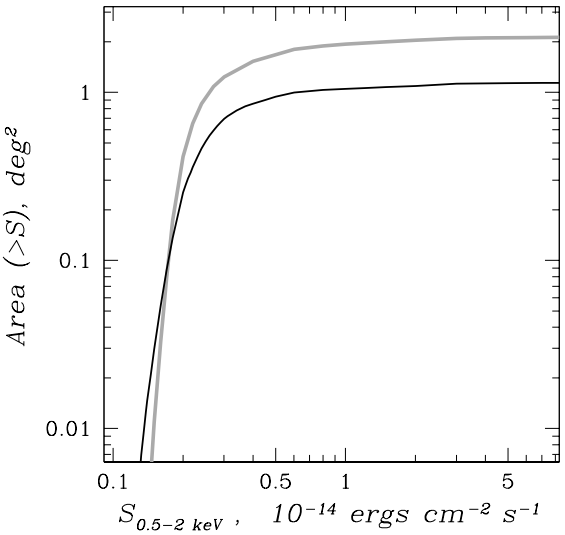

Figure 3. Survey area of SXDF (black curve) as a function of the total source flux in the 0.5–2 keV band. COSMOS flux-area curve corresponding to the results in Finoguenov et al. (2007) is shown as grey line.

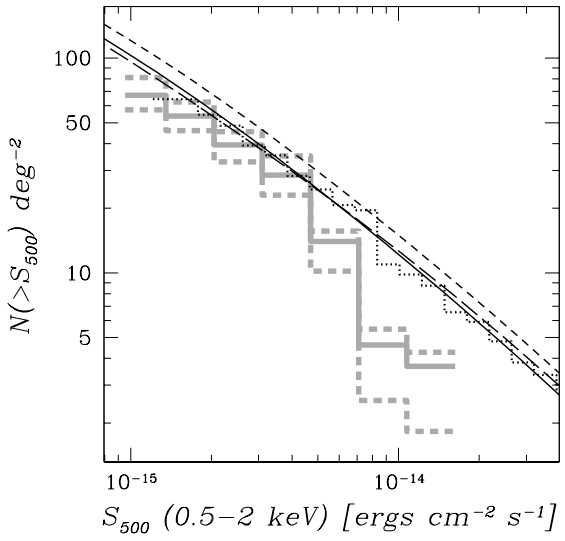

Figure 4. Cumulative cluster number counts ($\log(N > S) - \log(S)$) for the SXDF field. The solid grey histogram shows the data and dashed grey histograms denote the 68% confidence interval. The dotted histogram shows a $\log(N > S) - \log(S)$ of the COSMOS survey. The long dashed curve shows the prediction for no evolution in the luminosity function in Rosati et al. (2002), which provides a good fit to the date above 10^{-14} ergs s^{-1} cm^{-2} flux. The dashed line shows the WMAP5 predictions for $\log(N > S) - \log(S)$ under our assumptions for scaling relations and their evolution excluding. The solid line has been produced to match observational predictions by adopting a 5% reduction in σ_8.

5.1 Identification of X-ray jets and halo occupation statistics of radio-galaxies

Extensive Inverse Compton X-ray emission from large radio galaxies has been detected above redshift 1, such as 3C 356 (z=1.12; Simpson & Rawlings 2002), 3C 294 (z=1.786; Fabian et al. 2003), 6C 0905+39 (z=1.833 Erlund et al. 2008) and 4C 23.56 (z=2.48; Johnson et al. 2007). The flux of the emission depends on the energy density of the target photons, which in case of the CMB rises

as $(1+z)^4$ so canceling out the dimming expected from increased distance (Felten & Rees 1969; Schwartz 2002). Those studies predict a large number of extended sources detected in deep X-ray surveys, whose origin of the emission does not stem from the hot gas associated with potential wells of those systems, but is instead caused by the inverse Compton scattering of CMB photons on the relativistic electrons of a Mpc jet. However, there has not been a single survey, which can quantify the effect.

In order to carry out this study we use an expected match in the shape of the emission between the X-ray and radio source. The requirement for a match in the orientation between X-ray and radio elongation to within 10° substantially reduces a chance correspondence and is therefore used here to build the best-practice examples of such matches, which later can be used to treat more complex cases. We used the VLA survey of the field at 1.4 GHz to identify the radio sources (Simpson et al. 2006). The RMS of the image is 12–20μJ. There has been 14 complex morphology radio sources detected inside X-ray selected clusters in SXDF, all shown in Fig.5. Therefore a positional and azimuthal match is subject to a chance alignment of 0.7%, which can therefore be rejected with high confidence. With this method we have found three X-ray sources (IDs 25,28 and 70), which emission is entirely matched to a radio source. Three additional sources match substructure detected in the X-ray images (IDs 4, 39, 69) and the original sources had to be split (introducing new sources 90, 91 and 92 assigned to X-ray jets) to ensure unbiased flux estimates of both components. In case of cluster ID=69 and X-ray jet ID=92 the identification revealed different redshifts of the counterparts, therefore increasing the number of X-ray jets detected without detecting the cluster emission to 4 objects. This source has also been discussed in Geach et al. (2007) and Tu et al. (2009). All four objects also exhibit a match in spatial extent between radio and X-rays, which supports a physical link. The properties of the X-ray emission associated with radio jets are summarized in Tab.3. Column 1 lists object ID, columns 2 and 3 list the coordinates of center of X-ray emission, column 4 reports the spectroscopic redshift of the radio galaxy, column 5 reports the X-ray flux in units of 10^{-15} ergs cm^{-2} s^{-1} and column 6 displays the corresponding rest-frame luminosity in units of 10^{42} ergs s^{-1}. We used the power law model with photon index equal 2 in deriving the flux estimates and calculating the K-correction for X-rays and a $\alpha = 0.7$ index for the radio. Col (7) lists the radio counterpart in the catalog of Simpson et al. (2006), col (8) reports the flux (F_r) at 1.4GHz in mJy, col (9) reports the rest-frame radio luminosity (L_r) at 1.4GHz, calculated using the following formulae: $L_r = 4\pi D_L^2 F_r (1+z)^(\alpha-1)$. The luminosity distance (D_L) is calculated using the redshift listed in col. 4. The radio sources responsible for most of the IC emission are at the 10^{25} W/Hz level (the effect is detected from 20% of all such radio sources), which are characterized by the volume abundance of $\sim 10^{-6}$ Mpc^{-3} dex^{-1} at redshifts near 1. Comparison to theoretical model of Celotti & Fabian (2004), the IC effect detected in our survey is produced by the abundant sources at the faint end of the radio luminosity function they considered. This implies that the predictions in their Fig.3 need to be rescaled on X-axis by factor of 10. We can directly compute the required factor using our X-ray and radio measurements, as reported in col.(9). Indeed the obtained ratio is larger than 1. We have already dropped the factor associated with the assumption of the evolution of the magnetic field (which lowers the inferred X-ray flux for a given radio flux), which adds another factor of 4, so on average a factor of 10 stronger production of X-rays compared to a conservative assumption in Celotti & Fabian (2004) is observed. All six radio sources listed in Tab.3 are considered in detail as a part of the sample of Vardoulaki et al. (2008). At the same frequency, there is a good agreement with NVSS measurements and only one source (radio ID=7) has a steep spectrum (or much larger flux at lower frequencies compared to our estimate here). Thus, our conclusion on a factor of 10 stronger production of X-ray is neither an artifact, nor a result of using a different frequency band compared to Celotti & Fabian (2004).

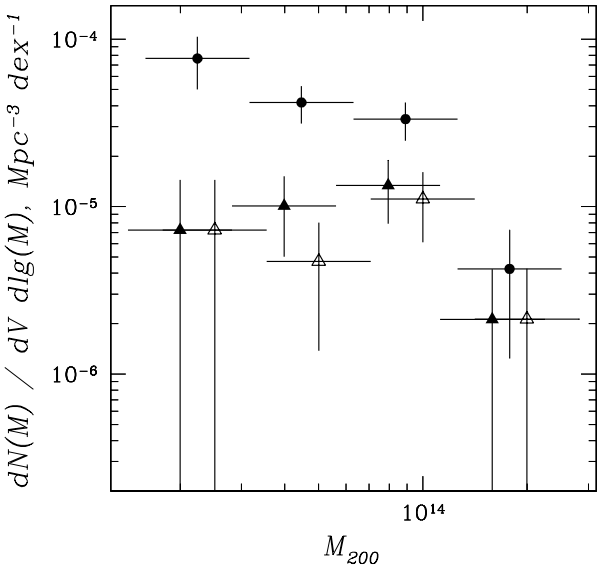

Figure 6. Mass function of $z < 1$ identified X-ray emitting halos (solid circles with error bars) and those selected to have a radio galaxy from a luminosity-limited sample. Solid triangles with error bars show halos with the spectroscopically confirmed radio galaxies within r_{200} and open triangles with error bars show matching within $0.2r_{200}$, but keeping the galaxies with consistent photometric redshift estimate but having no spectroscopic information.

One of the X-ray jets is remarkably bright in X-rays (ID 25). It would be the most luminous cluster in the field, while an optical counterpart is barely detected. The X-ray jet is located near an X-ray detected group into which its host is probably accreting. The X-ray luminosity of the dominant group is an order of magnitude fainter than that of the X-ray jet. In Fig.5 we present all 14 complex morphology radio sources located inside the extended X-ray emission.

In comparing the radio galaxy catalog to the catalog of X-ray clusters we note that a number of these sources match and the chances for the X-ray cluster to host a radio galaxy seem to increase with cluster mass. In order to characterize that we used our modeling of the survey to compute both the mass function of the full sample and the mass function of X-ray clusters that host a radio galaxy. We have excluded the 4 cases where X-ray emission is caused by IC. In calculating the mass function, we take into account the volume of the survey towards each cluster mass. For radio galaxies, we select the luminosity-limited sample of $L_{1.4GHz} > 5 \times 10^{23}$ W/Hz, which is valid to z of 1, given our flux limit of 100μJy. We therefore restricted the cluster selection and volume computation to a redshift of 1. The limiting luminosity is located in the radio source population dominated by FR I's (core brightened), which therefore justifies our use of limits for a point source. Finally, since spectroscopic identification of radio catalog is not complete, we calculate two examples of matching: one is by taking the spectroscopically identified radio galaxies with redshifts matching that of the cluster

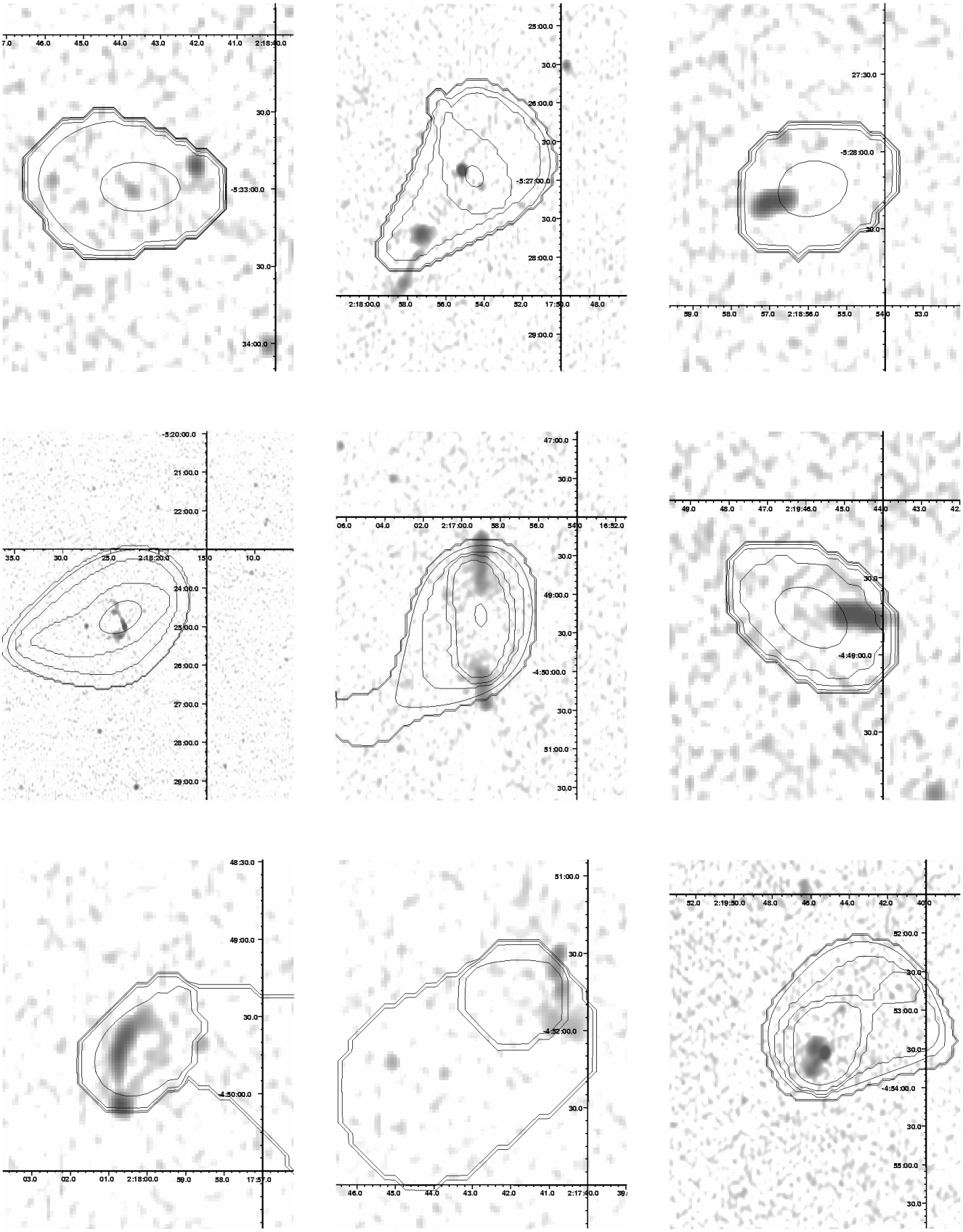

Figure 5. Comparison of complex radio sources with extended X-ray emission in SXDF. Images at 1.4 GHz frequency are overlaid with contours showing the wavelet reconstruction of extended X-ray emission on spatial scales of 32″, 64″, and 128″. From upper left to lower right the cluster IDs are

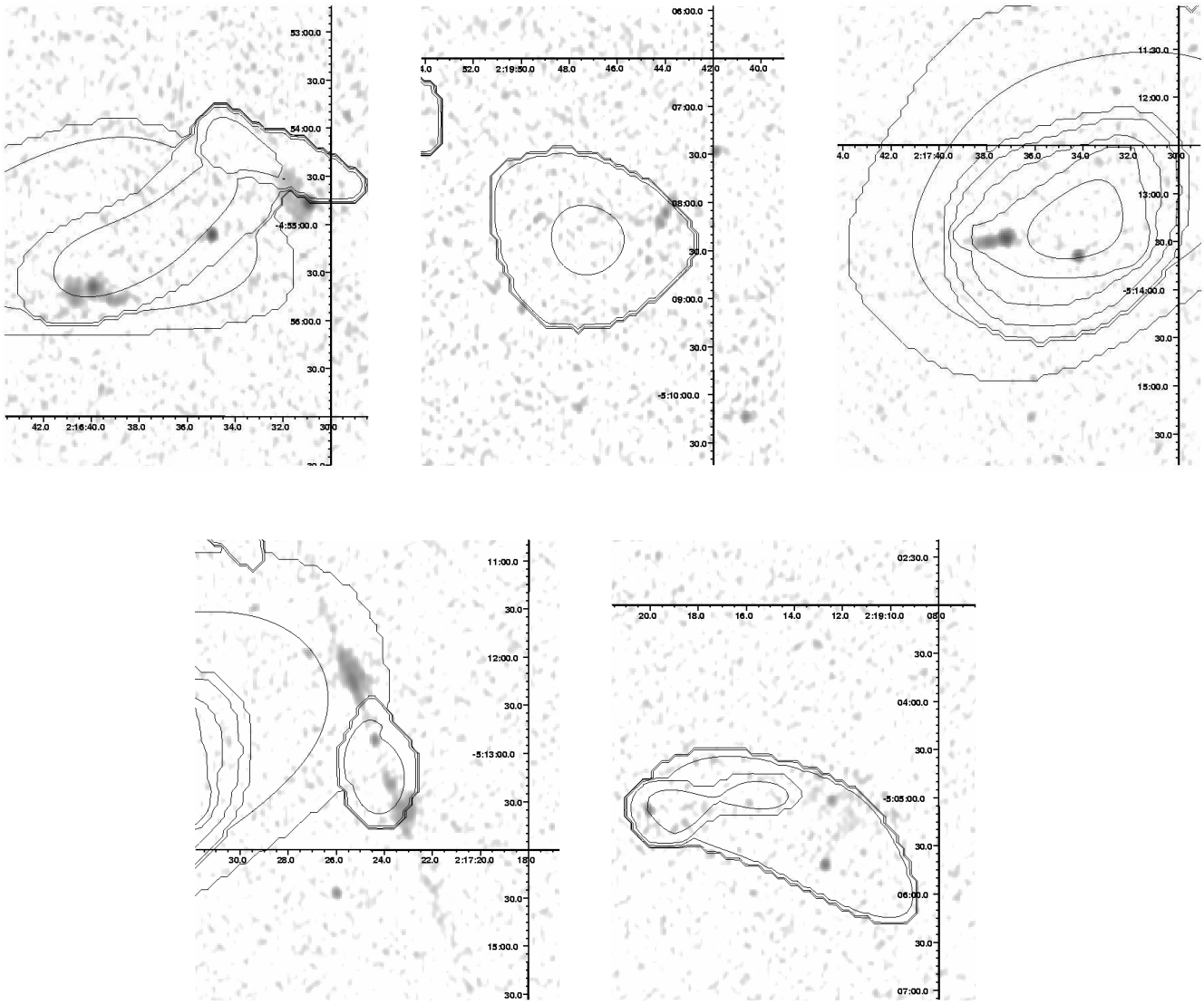

Figure 5. Continued... From upper left to lower right the cluster IDs are 39, 57, 69, 70, 84.

and the other is by assuming that once the radio galaxy is located within the $0.2r_{200}$ it belongs to the cluster. There 15 galaxies in total that fulfil this criterium, and after applying the radio luminosity threshold there is 9 left, which we used to compute the marked mass function. Only one system has a photometric redshift for the radio galaxy, but the galaxy is also on the red-sequence, suggesting that the association is real. The results are quantitatively similar and demonstrate in Fig.6 that indeed the probability to observe a radio galaxy increases with mass of the halo. These results of a direct HOD determination for radio AGNs are in good agreement with clustering analysis of 2SLAQ LRG survey (Wake et al. 2008), performed at redshifts near 0.6 and a similar selection of radio power.

5.2 Cluster counts

It is common to characterize a cluster survey by its area as a function of the limiting flux (which we do in Fig.3) and present the results as a relation between a cumulative surface density of clusters above a given flux limit vs the flux value, the cluster $\log(N > S) - \log(S)$ (e.g. Rosati et al. 1998). The details of our calculation, which is shown in Fig.4, are outlined in Finoguenov et al. (2007). In addition to the 57 identified sources, 9 sources were located in the area with insufficient optical data due to either survey geometry or a presence of the bright star. In calculation of the upper limit on the $\log(N > S) - \log(S)$ we have added those sources using the typical flux extrapolation for our apertures of 1.2. Sources identified as X-ray counterparts of radio jets were not considered for $\log(N > S) - \log(S)$. 11 sources locate within the area of best photometric data, but still lacking identification, were not considered in the $\log(N > S) - \log(S)$. The computed uncertainties in $\log(N > S) - \log(S)$ are purely statistical. The comparison of the $\log(N > S) - \log(S)$ to COSMOS results of Finoguenov et al. (2007) reveals a good agreement at low fluxes, while at fluxes exceeding 5×10^{-15} there is a lack of sources in the SXDF, compared to most previous surveys. The variation of a statistics of bright sources is driven by the sample variance in such fields (Hu &

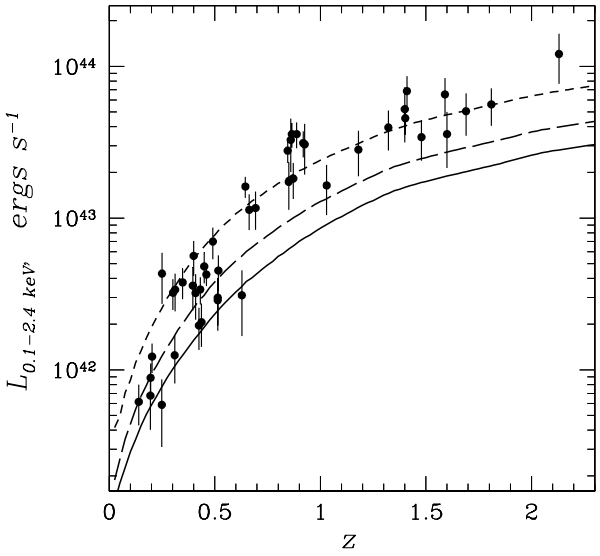

Figure 7. Illustration of the cluster luminosity probed as a function of cluster redshift in the SXDF. Filled circles represent the detected clusters with error bars based on the statistical errors in the flux measurements only. Short-dashed, long-dashed and solid black lines show the flux detection limits of -14.5dex -14.8dex and -15.0dex associated with 90, 50 and 10% of the total area, respectively.

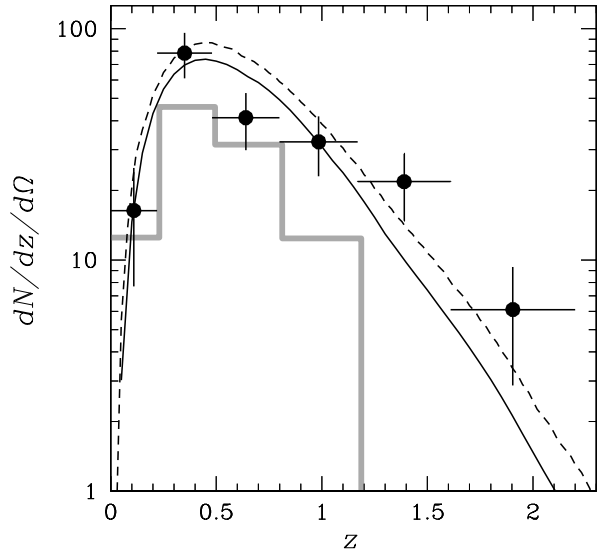

Figure 8. Differential redshift distribution ($dN/dz/d\Omega$ per square degree) of 57 identified X-ray groups and clusters of galaxies in the SXDF (points with error bars). The thick grey histogram shows the spectroscopically confirmed systems. Short-dashed black curve shows the model prediction adopting WMAP5 cosmology. Solid line shows the WMAP5 prediction with a reduced by 5% value of σ_8. Similar to Fig.4, we are accounting for the incomplete identification by the 20% upward correction for the data.

Kravtsov 2003) and is very important for the field-to-field comparison (e.g. McCracken et al. 2007) on how clustering affects the conclusions regarding galaxy evolution. We present the previous modeling of the $\log(N > S) - \log(S)$ of Rosati et al. (2002), which describes well the cluster counts above 10^{-14} ergs cm^{-2} s^{-1}. The short-dashed line is result of combining the adopted scaling relations, WMAP5 concordance cosmology (Komatsu et al. 2009) and a cosmological code of Peacock (2007). Since it clearly overpredicts the observed counts and previously published cluster counts, we considered the effect of excluding low-luminosity ($L_x < 10^{42}$ ergs s^{-1}) or high-redshift clusters ($z > 1.2$) or both. None of these attempts were successful in providing a satisfactory solution. In order to match the observations, we adopted a 5% lower value of σ_8, with a corresponding model prediction shown as a solid line. The role of SXDF in implying a change in the cosmological parameters, is however moderate, since the small size of the field causes large deviations at the bright end of the $\log(N > S) - \log(S)$.

5.3 Sample characteristics

In Fig. 7 we plot the observed characteristics of the SXDF cluster sample together with detection limits implied by both survey depth and our approach to search for clusters of galaxies.

In Fig. 8 we report the redshift distribution of the identified X-ray structures and attempt its modelling, assuming WMAP5 cosmology and using the adopted scaling relations and their evolution. Compared to a summary of scaling relations, presented in Finoguenov et al. (2007), we adopted a direct $L_X - M$ calibrations of Rykoff et al. (2008), which match well the results of COSMOS (Leauthaud et al. 2009). To compute the K-correction, we still need $L - T$ relation, for which we adopt

$$kT/keV = 0.2 + 6 \times 10^{(lg(L_X/E_z/ergs/s)-44.45)/2.1)} \quad (1)$$

and a fixed metalicity of 0.3 solar. The procedure for the flux extrapolation is the same as in Finoguenov et al. (2007). The WMAP5 concordance model prediction for the dN/dz is shown in Fig. 8 as a dashed curve and our best fit model to log(N)–log(S) data is shown as solid curve. We show the results of our spectroscopic follow-up (grey histogram) and account for incompleteness in our red sequence identification by increasing the counts by a factor of 1.2, which accounts for the area with lack of optical data. Removing the contribution of low luminosity ($L_X < 10^{42}$ ergs s^{-1}) systems produces negligible result. The largest deviation between the data and the model is the lack of clusters in the 0.6–1. redshift range, which can also be seen in Fig.7. The follow-up of the candidates (summarized as a grey histogram in Fig. 8) is quite complete at those redshifts, so it might be an effect of large-scale structure and shall be investigated further through a comparison to other surveys like COSMOS. The number of missing clusters at those redshifts is around 10 similar to the deficit on $\log(N > S) - \log(S)$ at high fluxes. The number of our high-z candidates is consistent with the cosmological expectation.

5.4 X-ray luminosity function

The procedure of calculating the luminosity function is similar to COSMOS (Finoguenov et al. 2007).

In Fig. 9 we present the luminosity function of SXDF clusters in the $0.2 < z < 1$ and $1 < z < 2.5$ redshift range. The choice of low redshift of 0.2 is due to incompleteness of the follow-up at low redshifts and we also make an upward correction of the data by 1.2 accounting for incomplete coverage of the X-ray data by the optical data. The SXDF results for the $0.2 < z < 1$ compares well to the COSMOS results in the $0 < z < 1.2$ range, which are also shown in the figure (dashed line). In Fig. 9 we also show the prediction of our cosmological modelling and the assumed scaling relations. The

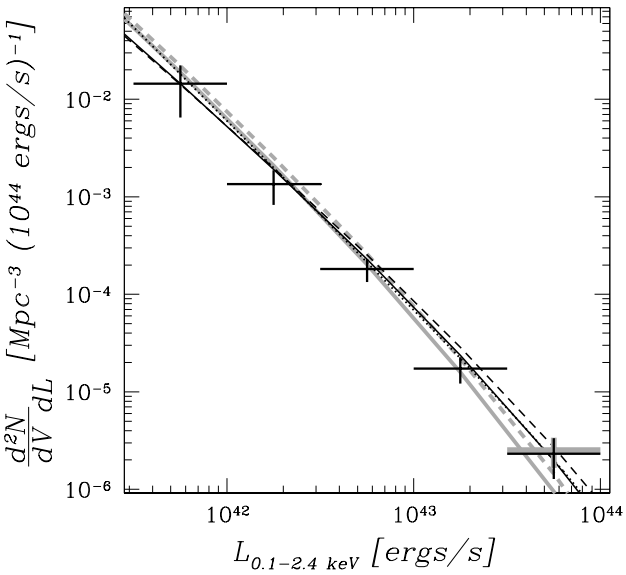

Figure 9. Luminosity function of clusters in the SXDF field. Black crosses indicate the data in the redshift range 0.2–1.0 and grey point shows the data in the redshift range 1–2.5, which is the first measurement reported for $z > 1$. We apply the 20% upward correction for incompleteness of cluster identification of the field. The dotted line shows the best fit to the COSMOS data over $0 < z < 1.2$ (Finoguenov et al. 2007). The dashed lines shows the WMAP5 prediction for the luminosity function in the 0–1 (black) and 1–2.5 (grey) redshift range. Solid lines shows the change in the model due to a 5% reduction in σ_8 value.

model describes well both the luminosity function, and its redshift evolution.

We have tested the effects of log-normal scatter on the luminosity function with $\delta lg(L_X) = 0.2$ (Vikhlinin et al. 2009) and found them to be important only at $L_x > 10^{44}$ ergs s^{-1}.

The sensitivity towards an assumption of σ_8 value is not so large for low-mass systems, and in consistency with previous tests, we show the prediction of a 5% reduced value of σ_8 in Fig. 9 (solid line). So, it is difficult to see if a particular part of XLF is causing a requirement for lowering the σ_8 value. Changing Ω_m value would require a self-consistent recalibration of data, which is beyond the scopes of this work, while the current dataset is sensitive only to changes in Ω_m exceeding 10%. Using galaxy groups one can break the degeneracy between Ω_M and σ_8 present in fitting the cluster counts. The biggest remaining uncertainty is scatter in the scaling relations for galaxy groups, which is not well known.

6 CONCLUSIONS

We have searched for extended X-ray emission in the SXDF and presented the catalog of identified X-ray groups and clusters of galaxies. Our analysis of the extended X-ray emission in the Subaru-XMM Deep Field revealed a new class of sources, associated with the inverse Compton emission from radio lobes. For extended objects identified as galaxy clusters, we derive the statistical properties of the survey and compare them to published results on COSMOS (Finoguenov et al. 2007) and the prediction of current best-fit cosmology and cluster scaling relations. We considered $\log(N > S) - \log(S)$, dn/dz and XLF tests. $\log(N > S) - \log(S)$ test showed that SXDF lack extended X-ray sources brighter than 5×10^{-15} ergs cm^{-2} s^{-1}, compared to other surveys, which we attribute to sample variance. XLF is in good agreement with COSMOS and is well modelled, but somewhat more uncertain due to incompleteness of the identification in SXDF field. Comparing the WMAP5 cosmology together with the scaling relations for clusters to the cluster counts, we detect a sensitivity of the sample towards present uncertainty in the cosmological parameters and illustrate it by changing the value of σ_8 by 5% to provide a best fit to our data and showing the change in the prediction for both $\log(N > S) - \log(S)$, dn/dz and XLF tests.

7 ACKNOWLEDGMENTS

In Germany, the XMM–Newton project is supported by the Bundesministerium fuer Wirtschaft und Technologie/Deutsches Zentrum fuer Luft- und Raumfahrt (BMWI/DLR, FKZ 50 OX 0001). Part of this work was supported by the Deutsches Zentrum für Luft– und Raumfahrt, DLR project numbers 50 OR 0207 and 50 OR 0405. AF acknowledges support from Spitzer UDS Legacy program to UMBC. AF thanks Andy Fabian for useful discussions regarding the X-ray jets. AF thanks the University of Leicester for the hospitality during his frequent visits. The authors thank the referee for useful comments on the manuscript.

REFERENCES

Bauer F. E., et al., 2002, AJ, 123, 1163
Bower, R. G., Lucey, J. R., & Ellis, R. S. 1992, MNRAS, 254, 601
Blakeslee, J.P., Franx, M., Postman, M. et al., 2003, ApJ, 596, 143
Böhringer, H., Collins, C. A., Guzzo, L., et al. 2002 ApJ, 566, 93
Borgani, S., Guzzo, L., 2001, Nature 409, 39
Bruzual, G., & Charlot, S. 2003, MNRAS, 344, 1000
Burenin R. A., Vikhlinin A., Hornstrup A., Ebeling H., Quintana H., Mescheryakov A., 2007, ApJS, 172, 561
Celotti A., Fabian A. C., 2004, MNRAS, 353, 523
Cirasuolo M., et al., 2007, MNRAS, 380, 585
Erlund M. C., Fabian A. C., Blundell K. M., 2008, MNRAS, 386, 1774
Fabian A. C., Sanders J. S., Crawford C. S., Ettori S., 2003, MNRAS, 341, 729
Felten J. E., Rees M. J., 1969, Natur, 221, 924
Foucaud S., et al., 2007, MNRAS, 376, L20
Furusawa H., et al., 2008, ApJS, 176, 1
Geach J. E., Simpson C., Rawlings S., Read A. M., Watson M., 2007, MNRAS, 381, 1369
Giacconi R., et al., 2002, ApJS, 139, 369
Giodini S., et al., 2009, ApJ, in press (arXiv:0904.0448)
Finoguenov A., Streblyanska A., Hasinger G., Hashimoto Y., Szokoly G., 2005, AdSpR, 36, 710
Finoguenov A., et al., 2007, ApJS, 172, 182
Finoguenov A., et al., 2009, ApJ, 704, 564
Jansen, F., Lumb D., Altieri, B., et al. 2001, A&A, 365, L1
Hu W., Kravtsov A. V., 2003, ApJ, 584, 702
Johnson O., Almaini O., Best P. N., Dunlop J., 2007, MNRAS, 376, 151
Kirsch, M. G. F., et al. 2004, SPIE, 5488, 103
Kodama, T., & Arimoto, N. 1997, A&A, 320, 41
Komatsu E., et al., 2009, ApJS, 180, 330
Leauthaud A., et al., 2009, ApJ, in press, (arXiv:0910.5219)
Lidman, C., Rosati, P., Demarco, R., et al., 2004, A&A, 416, 829
Lidman C., et al., 2008, A&A, 489, 981

Lonsdale C. J., et al., 2003, PASP, 115, 897
Mei, S., et al. 2006, ApJ, 644, 759
McCracken H. J., et al., 2007, ApJS, 172, 314
Pacaud F., et al., 2007, MNRAS, 382, 1289
Peacock J. A., 2007, MNRAS, 379, 1067
Rosati, P., della Ceca, R., Norman, C., & Giacconi, R. 1998, ApJL, 492, L21
Rosati, P., Borgani, S., & Norman, C. 2002, ARAA, 40, 539
Rykoff E. S., et al., 2008, MNRAS, 387, L28
Saxton, R. D., et al. 2005, 5 years of Science with XMM-Newton, 149
Schwartz D. A., 2002, ApJ, 569, L23
Silverman J. D., et al., 2009, ApJ, 695, 171
Simpson C., Rawlings S., 2002, MNRAS, 334, 511
Simpson C., et al., 2006, MNRAS, 372, 741
Snowden S. L., Mushotzky R. F., Kuntz K. D., Davis D. S., 2008, A&A, 478, 615
Smail I., Sharp R., Swinbank A. M., Akiyama M., Ueda Y., Foucaud S., Almaini O., Croom S., 2008, MNRAS, 389, 407
Smith, R. K., Brickhouse, N. S., Liedahl, D. A., & Raymond, J. C. 2001, ApJL, 556, L91
Stanford S. A., Eisenhardt P. R., Dickinson M., 1998, ApJ, 492, 461
Strazzullo, V., et al. 2006, A&A, 450, 909
Strüder L., Briel U.G., Dennerl K., et al. 2001, A&A, 365, L18
Tanaka, M., Kodama, T., Arimoto, N., Okamura, S., Umetsu, K., Shimasaku, K., Tanaka, I., & Yamada, T. 2005, MNRAS, 362, 268
Tanaka, M., Kodama, T., Kajisawa, M., Bower, R., Demarco, R., Finoguenov, A., Lidman, C., & Rosati, P. 2007, MNRAS, 377, 1206
Tanaka M., et al., 2008, A&A, 489, 571
Tu H., et al., 2009, A&A, 501, 475
Turner, M. J. L., et al. 2001, A&A, 365, L27
Ueda Y., et al., 2008, ApJS, 179, 124
van Breukelen C., et al., 2007, MNRAS, 382, 971
van Breukelen, C., et al. 2009, MNRAS, 395, 11
Vardoulaki E., Rawlings S., Simpson C., Bonfield D. G., Ivison R. J., Ibar E., 2008, MNRAS, 387, 505
Vikhlinin A., et al., 2009, ApJ, 692, 1033
Watson, M. G., et al. 2001, A&A, 365, L51
Watson M. G., et al., 2009, A&A, 493, 339
Wake D. A., Croom S. M., Sadler E. M., Johnston H. M., 2008, MNRAS, 391, 1674
Warren, S. J., Hambly, N. C., Lawrence, A., et al. 2009, MNRAS, in preparation
Yamada, T., et al. 2005, ApJ, 634, 861
Zhang, Y.-Y., Finoguenov, A., Böhringer, H., et al. 2004, A&A, 413, 49

Table 1. Catalog of the SXDF X-ray selected galaxy groups.

ID	R.A	Decl.	z	flux 10^{-14}	$L_{0.1-2.4keV}$	M_{200}	r_{200}			flux	red sequence		median	Ueda
	Eq.2000			ergs cm^{-2} s^{-1}	10^{42} ergs s^{-1}	10^{13} $M_\odot$	$'$	flag	N(z)	significance		redshift	photo-z	ID
(1)	(2)	(3)	(4)	(5)	(6)	(7)	(8)	(9)	(10)	(11)	(12)	(13)	(14)	(15)
SXDF01XGG	34.68284	-5.54973	0.378	1.11±0.19	8.95±1.54	7.30±0.73	2.5	2	6	5.8	7.6	$0.29^{+0.05}_{-0.05}$	0.40	0876 0889
SXDF03XGG	34.33485	-5.48511	0.382	1.32±0.33	10.94±2.72	8.21±1.17	2.5	1	5	4.0	2.3	$0.22^{+0.03}_{-0.06}$	0.35	
SXDF04XGG	34.47560	-5.45160	0.693	0.31±0.09	11.69±3.30	6.55±1.05	1.5	2	3	3.4	8.7	$0.61^{+0.05}_{-0.06}$	0.70	0621
SXDF06XGG	34.73260	-5.47054	0.451	0.52±0.12	6.52±1.51	5.68±0.76	2.0	1	4	4.3	8.5	$0.35^{+0.06}_{-0.03}$	0.45	0934
SXDF07XGG	34.60464	-5.41436	0.646	0.84±0.13	24.67±3.82	10.68±0.96	1.9	1	6	6.5	8.4	$0.56^{+0.04}_{-0.07}$	0.65	0784
SXDF08XGG	34.36312	-5.41925	0.645	0.51±0.08	15.49±2.48	8.09±0.75	1.7	2	3	6.4	5.3	$0.53^{+0.05}_{-0.04}$	0.65	
SXDF10XGG	34.19894	-4.55896	0.409	0.32±0.11	3.21±1.07	3.84±0.72	1.9	3	2	2.9	1.5	$0.30^{+0.03}_{-0.01}$	0.40	
SXDF14XGG	34.49784	-4.63107	0.396	0.42±0.13	3.88±1.22	4.35±0.78	2.0	5	2	3.2	3.3	$0.30^{+0.03}_{-0.10}$	0.35	
SXDF15XGG	34.23301	-4.65666	0.437	0.18±0.05	2.06±0.64	2.88±0.51	1.6	1	1	3.6	4.7	$0.34^{+0.06}_{-0.12}$	0.40	
SXDF16XGG	34.35674	-4.65945	0.196	0.55±0.13	0.92±0.22	2.15±0.30	2.8	1	3	4.2	1.9	$0.15^{+0.02}_{-0.02}$	0.25	0453
SXDF18XGG	34.53927	-4.67350	0.312	0.69±0.19	3.39±0.94	4.30±0.68	2.4	2	2	3.6	2.8	$0.27^{+0.02}_{-0.04}$	0.30	

The rest of the table will be released after acceptance of the paper

[a] – stellar halo

Table 2. Spectroscopic redshifts of cluster member galaxies.

R.A	Decl.	z	cluster
Eq.2000			ID
(1)	(2)	(3)	(4)
34.672458	-5.534833	0.381	1
34.675250	-5.547528	0.381	1
34.678875	-5.580494	0.375	1
34.681125	-5.553822	0.375	1
34.690000	-5.545900	0.375	1
34.690667	-5.548917	0.383	1
34.315625	-5.488881	0.382	3
34.328500	-5.491192	0.381	3
34.332292	-5.502233	0.383	3
34.333792	-5.492828	0.381	3
34.359750	-5.507003	0.383	3
34.488667	-5.465550	0.694	4
34.470042	-5.438756	0.695	4
34.475771	-5.451581	0.690	4
34.735500	-5.472017	0.452	6
34.737667	-5.472025	0.450	6
34.745083	-5.497194	0.453	6
34.758708	-5.467483	0.450	6
34.579429	-5.396031	0.646	7
34.588342	-5.421225	0.643	7
34.598000	-5.416903	0.647	7
34.604929	-5.421614	0.646	7
34.607771	-5.422281	0.647	7
34.612500	-5.418975	0.646	7
34.346642	-5.405492	0.644	8
34.346871	-5.414247	0.643	8
34.375917	-5.425039	0.648	8
34.202500	-4.555364	0.409	10
34.204000	-4.555958	0.409	10
34.489558	-4.650786	0.394	14
34.513667	-4.625025	0.397	14
34.239917	-4.664153	0.437	15
34.352625	-4.662078	0.197	16
34.359542	-4.659900	0.195	16
34.361042	-4.662269	0.196	16
34.531042	-4.682667	0.314	18
34.544083	-4.710425	0.310	18
Abridged			

Table 3. Properties of extended X-ray emission associated with radio jets.

ID host cluster (1)	R.A Eq.2000 (2)	Decl. Eq.2000 (3)	z (4)	flux 10^{-15} ergs cm^{-2} s^{-1} (5)	$L_{0.5-2keV}$ 10^{42} ergs s^{-1} (6)	Simpson ID (7)	Flux 1.4GHz, mJy (8)	$L_{1.4GHz}$ 10^{23} W/Hz (9)	$L_x\nu_x/L_r\nu_r$ $\times(1+z)^{-3.7}$ (10)
SXDF90XGG	34.47560	-5.45160	0.693	1.66 ± 0.50	3.6±1.1	19	4.83	87 ± 1	4.2
SXDF25XGG	34.24682	-4.82231	1.179	6.85 ± 0.91	54.±7.1	7	9.6	605 ± 2	3.6
SXDF28XGG	34.49991	-4.82799	0.192	1.24 ± 0.37	0.14±0.04	20	4.6	4.4 ± 0.02	12.
SXDF91XGG	34.14713	-4.91255	0.865	0.74 ± 0.27	2.8±1.0	12	6.59	200 ± 1	1.0[a]
SXDF92XGG	34.39369	-5.22180	0.645	0.80 ± 0.23	1.5±0.4	33	2.37	36 ± 0.4	4.7
SXDF70XGG	34.35118	-5.21950	0.919	1.89 ± 0.34	8.2±1.5	18	4.84	170 ± 1	3.1

[a] – only one radio lobe is used in the X-ray estimate